

**Synergistic Catalyst-Support Interactions in a Graphene-Mn<sub>3</sub>O<sub>4</sub>  
Electrocatalyst for Vanadium Redox Flow Batteries**

*Andinet Ejigu, Matthew Edwards and Darren A. Walsh\**

School of Chemistry, The University of Nottingham, Nottingham NG7 2RD, UK

E-mail: [darren.walsh@nottingham.ac.uk](mailto:darren.walsh@nottingham.ac.uk);

Tel: +44 115 8467495; Fax: +44 115 9513562

## ABSTRACT

The development of vanadium redox flow batteries (VRFBs) is partly limited by the sluggishness of the electrochemical reactions at conventional carbon-based electrodes. The  $\text{VO}^{2+}/\text{VO}_2^+$  redox reaction is particularly sluggish and improvements in battery performance require the development of new electrocatalysts for this reaction. In this study, synergistic catalyst-support interactions in a nitrogen-doped, reduced-graphene oxide/ $\text{Mn}_3\text{O}_4$  (N-rGO- $\text{Mn}_3\text{O}_4$ ) composite electrocatalyst for  $\text{VO}^{2+}/\text{VO}_2^+$  electrochemistry are described. X-ray photoelectron spectroscopy (XPS) and X-ray diffraction (XRD) confirm incorporation of nitrogen into the graphene framework during co-reduction of GO,  $\text{KMnO}_4$  and  $\text{NH}_3$  to form the electrocatalyst, while transmission electron microscopy (TEM) and XRD confirm the presence of *ca.* 30 nm  $\text{Mn}_3\text{O}_4$  nanoparticles on the N-rGO support. XPS analysis shows that the composite contains 27% pyridinic N, 42% pyrrolic N, 23% graphitic N and 8% oxidic N. Electrochemical analysis shows that the electrocatalytic activity of the composite material is significantly higher than those of the individual components due to synergism between the  $\text{Mn}_3\text{O}_4$  nanoparticles and the carbonaceous support material. The electrocatalytic activity is highest when the  $\text{Mn}_3\text{O}_4$  loading is ~24% but decreases at lower and higher loadings. Furthermore, electrocatalysis of the redox reaction is only observed when nitrogen is present within the support framework, demonstrating that the metal-nitrogen-carbon coupling is key to the performance of this electrocatalytic composite for  $\text{VO}^{2+}/\text{VO}_2^+$  electrochemistry.

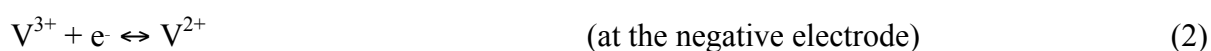
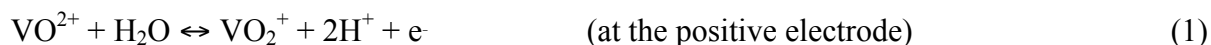
**Keywords:** redox flow battery; energy; electrocatalysis; graphene; cyclic voltammetry

## Introduction

Escalating CO<sub>2</sub> emissions, and the widespread desire to reduce our reliance on fossil fuels, are leading to a rapid growth in the development of renewable energy technologies that can contribute to the future energy mix. Wind and solar energy currently contribute about 4% of the total global electricity production but this is expected to increase to 25% by 2030.<sup>1</sup> However, as the quantity of electricity generated by such technologies increases, it is crucial that methods for mediating the intermittency of such supplies are available. Electrochemical methods have much to offer in this respect and the development of electrochemical methods for producing (and using) storable fuels such as H<sub>2</sub> (from water splitting), and CO, formic acid, and methanol (from atmospheric CO<sub>2</sub>) using sustainable electricity are extremely active areas of research.<sup>2,3</sup> The storage (and subsequent release) of electrical energy in batteries is also expected to play a significant role in our sustainable energy future and devices such as advanced Li batteries and redox flow batteries (RFBs) are attracting a lot of attention.<sup>4,5</sup> Central to each of these electrochemical technologies are electrocatalytic reactions (*i.e.*, electrochemical reactions in which the rate of reaction depends on the composition of the electrode material) and in many cases, technological advances are limited by the availability and/or cost of effective electrocatalysts.

Of the electrochemical devices mentioned above, RFBs are particularly promising for grid-scale energy storage owing to their ability to store large amounts of energy, their flexibility of design, and their long lifetimes.<sup>6-8</sup> A typical RFB consists of two electrodes (typically carbon) separated by an ion-conducting porous membrane and two tanks containing redox electrolytes, which are pumped to electrolytic cell during charging and discharging. The most common electrolytes are based on aqueous acidic media although some groups have recently proposed using organic solvents<sup>9</sup> or room temperature ionic liquids<sup>10</sup> to increase the energy densities of RFBs. While a wide range of redox electrolytes

has been proposed for RFBs, the all-vanadium systems (VRFBs) invented by Skyllas-Kazacos are most popular as they contain the same element in the positive and negative electrolytes, mitigating the effects of cross contamination:<sup>1,7,11</sup>



Due to the effects of sluggish electron transfer in VRBs, the last few years has seen a rapid increase in the number of publications devoted to the development of novel electrocatalysts for each reaction.<sup>12-14</sup> The  $\text{VO}^{2+}/\text{VO}_2^+$  is particularly sluggish and also problematic is the fact that the range of electrocatalyst materials for this couple is limited due to its high redox potential (1.0 V), at which few materials are stable in acidic media.<sup>15</sup> While noble metals such as Pt could potentially be used in VRFBs, its high cost (and affinity for  $\text{H}_2$  evolution if also used at the negative electrode) hinder its widespread use.<sup>16</sup> A number of researchers have functionalized less-expensive carbon-based materials such as mesoporous carbons, carbon nanotubes and graphene with O- and N-containing groups to increase their electrocatalytic activities.<sup>17-22</sup> Some materials based on reduced graphene oxide (rGO) and GO have also been used,<sup>23,24</sup> and residual oxygenic functional groups in rGO can serve as electrocatalytic sites.<sup>20,25</sup> The electrocatalytic activity of rGO has been further improved by N-doping, which provides electrocatalytic binding and activation sites for the vanadium redox couples.<sup>18,26</sup> A somewhat separate area of research focuses on the development of metal oxide electrocatalysts, such as  $\text{Nb}_2\text{O}_5$ ,  $\text{WO}_3$ ,  $\text{Mn}_3\text{O}_4$ , and  $\text{TiO}_2$ , supported on high surface area carbons.<sup>27-29</sup> In particular, the promising electrocatalytic activity of  $\text{Mn}_3\text{O}_4$  supported on C felt electrodes has been clearly demonstrated by Kim<sup>29</sup> using cyclic

voltammetry but it has been pointed out that the durability of such catalysts in the acidic environment within VRFBs requires further exploration.<sup>12</sup>

An emerging and promising trend in electrocatalyst development is the exploitation of synergistic interactions between the electrocatalyst and electrocatalyst support. Such interactions result from the presence of dual active sites at the electrocatalyst-support interface.<sup>30-32</sup> Composite electrocatalysts consisting of various spinel metal oxides and N-rGO have demonstrated higher activities for the O<sub>2</sub> reduction reaction than either constituent alone and could lead to new developments in fuel cell technology.<sup>30,33,34</sup> In this paper, we describe electrocatalytic synergism in an N-doped rGO/Mn<sub>3</sub>O<sub>4</sub> electrocatalyst for vanadium redox electrochemistry. The electrocatalyst was formed by co-reducing GO, KMnO<sub>4</sub> and NH<sub>3</sub> and the electrocatalytic activity of the composite material was evaluated using cyclic voltammetry and electrochemical impedance spectroscopy. As we describe below, the electrocatalytic activities of free Mn<sub>3</sub>O<sub>4</sub> and N-rGO for VO<sup>2+</sup>/VO<sub>2</sub><sup>+</sup> electrochemistry are low compared to that of the composite material. In addition, we will show that the presence of N in the composite material is crucial to the performance of the synergistic electrocatalyst, and we discuss the optimum Mn<sub>3</sub>O<sub>4</sub> loading within the electrocatalyst. Finally, we will show that the hybrid electrocatalyst withstands an extended durability test in which its potential is repeatedly cycled, suggesting that this material could be very useful for the development of long-lifetime redox cells.

## Experimental Section

**Materials and Apparatus.** All chemicals were used as received. Electrochemical measurements were performed using a model 760C potentiostat (CH Instruments, Austin, TX). TEM images were recorded using a JEOL 2000FX microscope operated at 200 kV. SEM analysis was carried out using a Philips XL30 FEG environmental microscope operated

at 20 kV. Powder XRD analysis was performed using a Bruker D8 Advance powder diffractometer with Cu  $K_\alpha$  radiation ( $\lambda = 0.154$  nm) and operating at 40 kV and 40 mA. XPS was performed using a Kratos Axis Ultra spectrometer with a monochromated Al  $K_\alpha$  X-ray source ( $E = 1486.6$  eV), hybrid (magnetic/electrostatic) optics, a hemispherical analyzer and a multichannel plate and delay line detector (DLD) with an X-ray angle of incidence of  $30^\circ$  relative to the surface normal. Raman spectra were recorded using a Horiba–Jobin–Yvon LabRAM microscope, with a  $600$  lines  $\text{mm}^{-1}$  grating, a Synapse CCD detector and  $532$  nm laser operating at *ca.*  $40$  mW. The decomposition temperature of the samples was measured using TGA (Q500 V20.10 Build 36) on Pt pans under air at a ramp rate of  $10$   $^\circ\text{C min}^{-1}$ .

***Electrochemical Measurements.*** Electrochemical measurements were performed using a three-electrode cell consisting of a  $5$  mm-diameter glassy carbon (GC) disk working electrode, an Ag|AgCl reference electrode, and a Pt counter electrode (area =  $1.6$   $\text{cm}^2$ ). Before use, GC working electrodes were polished with aqueous  $0.3$   $\mu\text{m}$  alumina (Buehler, Lake Bluff, Illinois) slurries on felt polishing pads and rinsed with deionized water. Electrocatalyst inks were prepared by dispersing  $0.6$  mg of the desired material (*e.g.*, N-rGO-Mn<sub>3</sub>O<sub>4</sub>, rGO-Mn<sub>3</sub>O<sub>4</sub>, N-rGO, or Mn<sub>3</sub>O<sub>4</sub>) in a mixture of  $200$   $\mu\text{L}$  of deionised water and  $10$   $\mu\text{L}$  of Nafion (5 wt.%) in an ultrasonic bath for  $30$  min. GC electrodes were modified with  $10$   $\mu\text{L}$  of the appropriate ink and dried at room temperature in air. CVs were recorded in  $1.0$  M VOSO<sub>4</sub> +  $2.0$  M H<sub>2</sub>SO<sub>4</sub>, which was deoxygenated prior to use by bubbling with Ar for  $20$  min. A blanket of Ar was maintained above the electrolyte during measurements. In all cases, the measured currents were normalised to the geometric area of the GC disk. Electrochemical impedance spectroscopy (EIS) was performed in the frequency range  $100$  kHz -  $100$  mHz at an oscillation amplitude of  $5$  mV and applied potential of  $0.95$  V. Impedance spectra were fitted to Randles equivalent circuit model using Z-view software (Scribner Associates Inc.)

**Synthesis of GO, N-rGO, Mn<sub>3</sub>O<sub>4</sub>, and N-rGO-Mn<sub>3</sub>O<sub>4</sub>.** GO was synthesised according to the modified Hummer's method.<sup>35</sup> Briefly, a mixture consisting of 360 mL of 98% H<sub>2</sub>SO<sub>4</sub> and 40 mL of 85% H<sub>3</sub>PO<sub>4</sub> was added to a mixture of 3.0 g of graphite powder and 18 g of KMnO<sub>4</sub> and heated at 50 °C for 12 h. The mixture was allowed to cool to room temperature and was then mixed with ice (400 mL) and H<sub>2</sub>O<sub>2</sub> (3.0 mL, 35%). The suspension was then filtered to yield a dark brown solid, which was washed with HCl (200 mL, 30%) and then H<sub>2</sub>O (200 mL). After each wash, the mixture was centrifuged, the supernatant was decanted, and the remaining solid material was dried overnight in an oven at 70 °C. N-rGO-Mn<sub>3</sub>O<sub>4</sub> was synthesised using the method described in Reference 36; GO (100 mg) was dispersed in water (200 mL) and sonicated for 1 h. 10 mL of KMnO<sub>4</sub> (1 mg mL<sup>-1</sup>) and 1 mL of NH<sub>3</sub> (25%) were added to the GO suspension as it stirred. 1 mL of hydrazine hydrate was then added and the mixture was refluxed at 95 °C for 3 h under constant stirring. After cooling to room temperature, the product was collected by centrifugation, washed several times with water, and dried in an oven at 70 °C for 12 h. rGO-Mn<sub>3</sub>O<sub>4</sub> and N-rGO were synthesised using the same procedure but without the use of NH<sub>3</sub> and KMnO<sub>4</sub>, respectively. Mn<sub>3</sub>O<sub>4</sub> was synthesised by refluxing a mixture of KMnO<sub>4</sub> (aq) (200 mg) and hydrated hydrazine (4 mL) for 3 h at 95 °C. The product was centrifuged and washed several times with water.

## Results and discussion

### Characterisation of N-rGO-Mn<sub>3</sub>O<sub>4</sub> using XRD, Raman Spectroscopy and SEM.

XRD was first used to characterise the composite material and its individual components and the data are shown in Figure 1A. Prior to reduction, the (002) diffraction peak of GO appeared at 10.95°, corresponding to a distance between adjacent GO sheets of 0.75 nm, in agreement with published data.<sup>37,38</sup> Upon reduction, the (002) GO peak shifted to 24.8°,

corresponding to an interplane distance of 0.35 nm and demonstrating that reduction of the graphene surface groups reduces interplane repulsion. Figure 1B shows XRD patterns obtained for Mn<sub>3</sub>O<sub>4</sub> and N-rGO-Mn<sub>3</sub>O<sub>4</sub>. The Mn<sub>3</sub>O<sub>4</sub> patterns is consistent with that expected for tetragonal hausmannite (JCPDS 24-0734, grey line in Figure 1B)<sup>39</sup> and the N-rGO-Mn<sub>3</sub>O<sub>4</sub> composite pattern contains peaks due to the rGO and pure Mn<sub>3</sub>O<sub>4</sub>. A broad peak at  $2\theta = 24.8^\circ$  and a small peak at  $2\theta = 43^\circ$  were due to the disordered rGO layers.<sup>36</sup> The average size of the Mn<sub>3</sub>O<sub>4</sub> crystallites can be related to the width of the peaks by the Scherrer Equation:

$$t = \frac{K\lambda}{\beta \cos\theta} \quad (3)$$

where  $t$  is the mean crystalline size,  $\lambda$  is the X-ray wavelength,  $\beta$  is the full width at half maximum of the peak in radians,  $\theta$  is the Bragg angle at which the peak is observed, and  $K$  is the shape factor, which depends on the shape of the particle (0.9 is usually used for particles of unknown geometry). Using Equation 3, the mean Mn<sub>3</sub>O<sub>4</sub> crystallite size was estimated as 32.5 nm.

Figure 1C shows the Raman spectra of GO, Mn<sub>3</sub>O<sub>4</sub> and N-rGO-Mn<sub>3</sub>O<sub>4</sub>. The GO sample shows the typical D and G bands (associated with vibrational stretching of sp<sup>2</sup> carbons and sp<sup>3</sup> defect sites, respectively) at 1354 and 1601 cm<sup>-1</sup> respectively.<sup>40</sup> In the N-rGO-Mn<sub>3</sub>O<sub>4</sub> spectrum, the G band was approximately 10 cm<sup>-1</sup> lower than in the GO spectrum due to the interaction between C and N in the composite material.<sup>41</sup> The ratio of the intensity of the D band to that of the G band ( $I_D/I_G$ ) increased from 0.75 in the GO spectrum to 0.95 in that of the N-rGO-Mn<sub>3</sub>O<sub>4</sub>, indicating that incorporation of N into the graphene structure increased the extent of disorder and defect sites.<sup>42</sup> Finally, a sharp peak appeared at

656  $\text{cm}^{-1}$  in the  $\text{Mn}_3\text{O}_4$  and N-rGO- $\text{Mn}_3\text{O}_4$  spectra, which is due to an Mn-O stretching mode.<sup>43,44</sup>

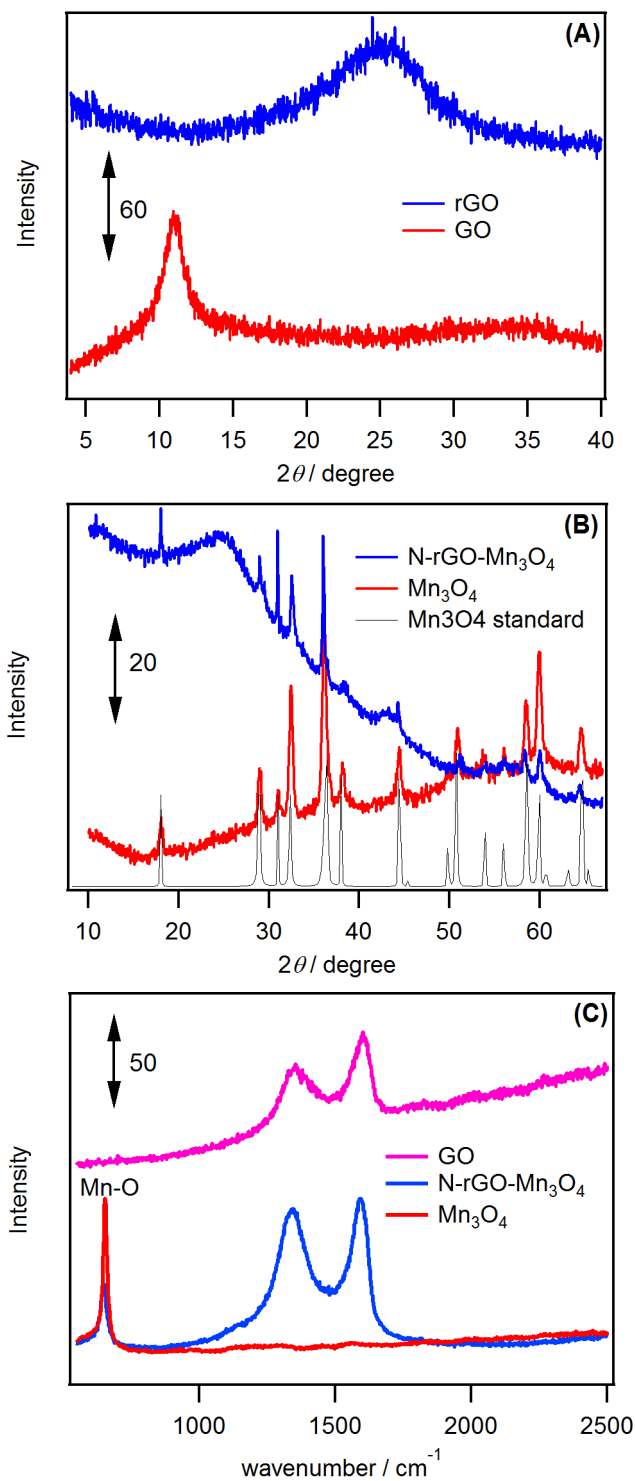


**Figure 1.** XRD patterns of (A) GO and rGO, and (B)  $\text{Mn}_3\text{O}_4$  and N-rGO- $\text{Mn}_3\text{O}_4$ . (C) Raman spectra of GO,  $\text{Mn}_3\text{O}_4$  and N-rGO- $\text{Mn}_3\text{O}_4$ .

SEM analysis of N-rGO-Mn<sub>3</sub>O<sub>4</sub> (Figure 2A) shows wrinkling in the graphene sheets, which can be attributed to the local stress caused by the introduction of N and the removal of O during reduction (an SEM image of the GO is shown in Figure S1 of the Supporting Information).<sup>18</sup> Figure 2B (and Figure S2 in the Supporting Information) shows that, in the absence of rGO, Mn<sub>3</sub>O<sub>4</sub> particles aggregated, whereas highly-dispersed Mn<sub>3</sub>O<sub>4</sub> nanoparticles were formed on the rGO sheets during reduction/co-deposition (Figures 2C and 2D). The average nanoparticles size was approximately 30 nm, which agrees well with that obtained using the XRD data and Equation 3.

**Characterisation of N-rGO-Mn<sub>3</sub>O<sub>4</sub> using XPS.** Figure 3A shows the wide-scan XP spectrum of N-rGO-Mn<sub>3</sub>O<sub>4</sub>, which consists of photoemissions from C, N, O and Mn. The presence of N in the spectrum shows that doping of N into the rGO composite was successful. The atomic concentrations of C, N, O and Mn in N-rGO-Mn<sub>3</sub>O<sub>4</sub> were 78.6%, 2.9%, 14.6% and 3.6%, respectively. High-resolution XP spectra of GO and N-rGO-Mn<sub>3</sub>O<sub>4</sub> in the C 1s region, with spectral fitting due to the contribution of O- and N- containing functional groups are shown in Figures 3B and 3C. The peak at 284.5 eV in the GO spectrum is attributed to sp<sup>2</sup> carbon, the most intense peak at 286.4 eV is attributed to C–O-containing functional groups, and the small shoulder at 288.3 eV is attributed to C=O- and O–C=O-containing species.<sup>36,45,46</sup> In comparison, the intensity of the sp<sup>2</sup> carbon in the N-rGO-Mn<sub>3</sub>O<sub>4</sub> spectrum was significantly higher, while the intensities of O-containing functional groups were significantly lower, than in the GO spectrum. The contribution of the C–O functional groups decreased from 50% in GO to 6% in N-rGO-Mn<sub>3</sub>O<sub>4</sub> while the contribution due to C=O/O–C=O functional groups decreased from 13% to 7% (Table S1 in the Supporting Information). This shows that hydrazine hydrate is effective in reducing C–O-containing functional groups and less effective at reducing C=O/O–C=O functional groups, and is

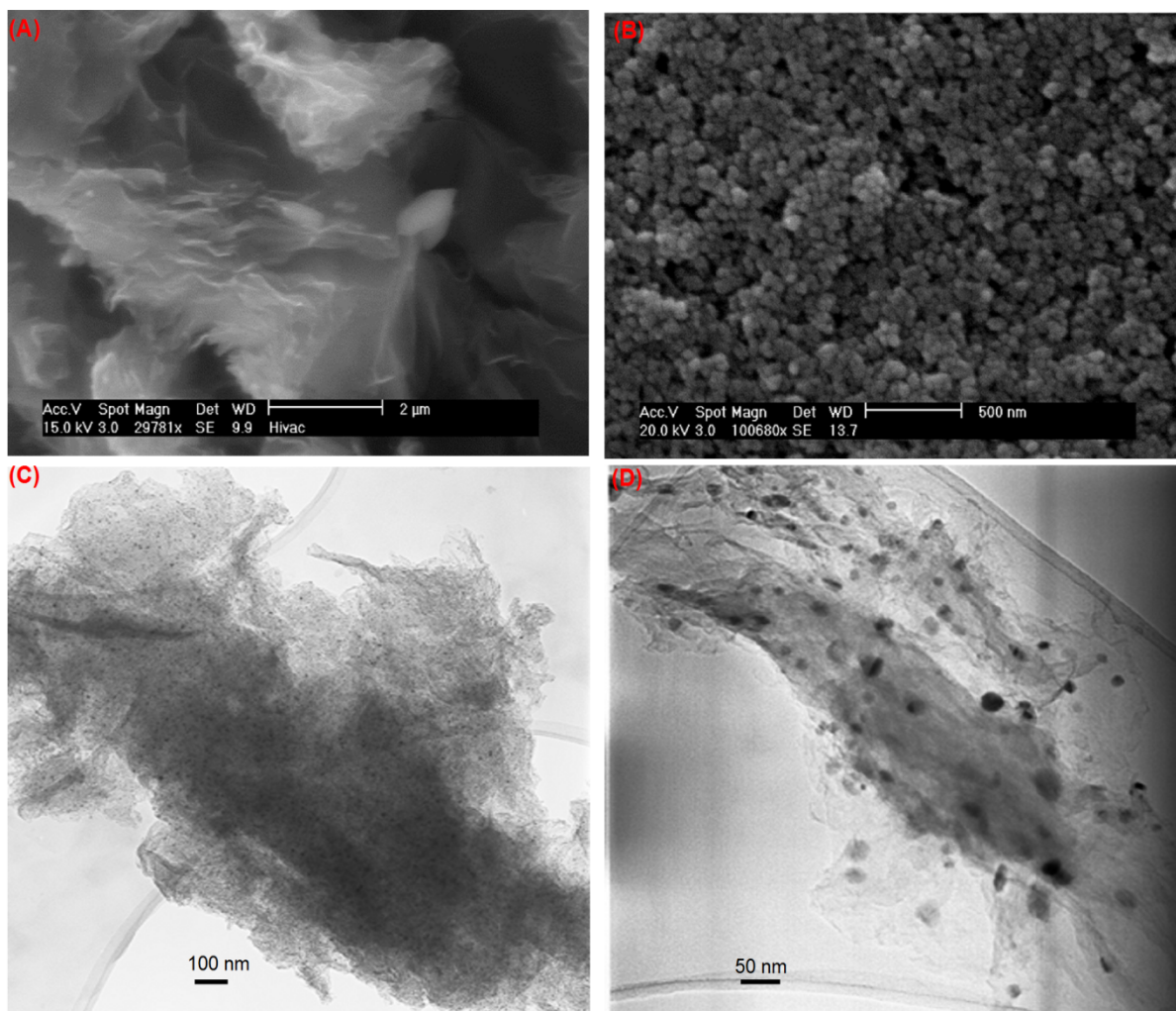


**Figure 2.** SEM image of (A) *N-rGO-Mn<sub>3</sub>O<sub>4</sub>*, and (B) *Mn<sub>3</sub>O<sub>4</sub>*. TEM images of *N-rGO-Mn<sub>3</sub>O<sub>4</sub>* are shown in C and D.

consistent with previous results.<sup>36</sup> A C–N feature appeared at 285.4 eV and the high resolution N 1s scan (Figure 3D) was deconvoluted into pyridinic N–C (27%), pyrrolic N–C (42%), graphitic N–C (23%), and oxidic-N (8%) contributions.<sup>41,45</sup> Graphitic N, in particular, is believed to be electrocatalytically active towards  $\text{VO}^{2+}/\text{VO}_2^+$ ,<sup>18</sup> and we will return to this topic in the next section.

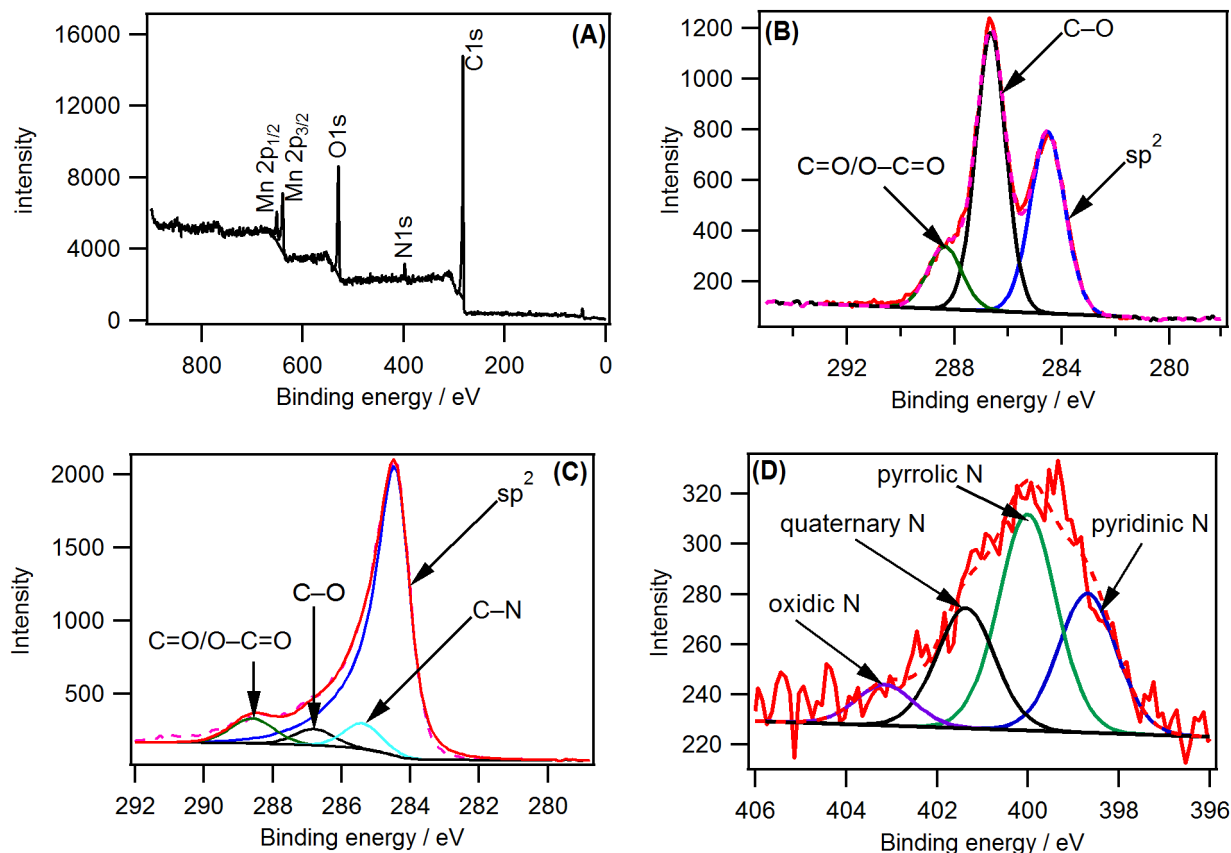


**Figure 3.** (A) Wide-scan XPS spectrum of *N*-rGO-Mn<sub>3</sub>O<sub>4</sub>. (B) High-resolution XPS spectrum of GO in the C 1s region. (C) High-resolution XPS spectrum of *N*-rGO-Mn<sub>3</sub>O<sub>4</sub> in the C 1s region. (D) High-resolution XPS spectrum of *N*-rGO-Mn<sub>3</sub>O<sub>4</sub> in the N 1s region. All peak positions were charge corrected by setting the binding energy of the C 1s signal to 285.5 eV.

It has been shown that Mn<sub>3</sub>O<sub>4</sub> can contain various Mn oxidation states such as Mn<sup>2+</sup> and Mn<sup>3+</sup> as in MnO-Mn<sub>2</sub>O<sub>3</sub> or Mn<sup>2+</sup> and Mn<sup>4+</sup> as in 2MnO-MnO<sub>2</sub>.<sup>47,48</sup> Figure 4 shows the high-resolution XPS spectra of the Mn 2p and Mn 3s regions obtained from XPS analysis of *N*-rGO-Mn<sub>3</sub>O<sub>4</sub>. The Mn 2p<sub>3/2</sub> peak was at 641.4 eV and the Mn 2p<sub>1/2</sub> peak was at 653.2 eV, giving a spin-orbit splitting of 11.8 eV, which is consistent with previously reported data for Mn<sub>3</sub>O<sub>4</sub>.<sup>36,49</sup> Moreover, the peak separation between Mn 2p<sub>3/2</sub> and the lowest component of O 1s (Figure S3 in the Supporting Information) is 111.6 eV, which is also consistent with the

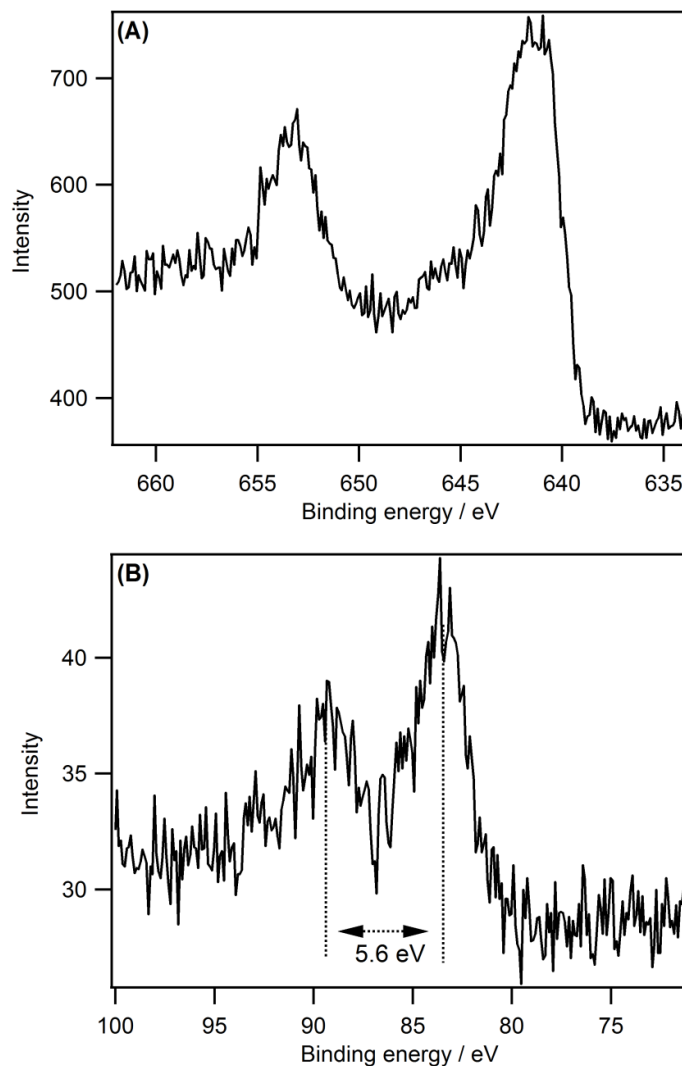


**Figure 4.** High resolution XP spectra of *N-rGO-Mn<sub>3</sub>O<sub>4</sub>* in the (A) Mn 2p and (B) Mn 3s regions.

reported value for the Mn–O moiety of Mn<sub>3</sub>O<sub>4</sub>.<sup>50</sup>

Splitting of the 3s signal (Figure 4B) was 5.6 eV and is due to the exchange coupling between the 3s hole (upon photoelectron ejection) and the 3d electrons. The magnitude the splitting can reveal the oxidation state of Mn<sup>48,50</sup> and splitting in MnO, Mn<sub>2</sub>O<sub>3</sub>, MnO<sub>2</sub> is 5.8 eV, 5.4 eV and 4.9 eV, respectively.<sup>50</sup> The observed splitting in our spectrum, which is in accordance with earlier reports for Mn<sub>3</sub>O<sub>4</sub>,<sup>51</sup> suggests that *N-rGO-Mn<sub>3</sub>O<sub>4</sub>* contained a mixture of Mn<sup>2+</sup> and Mn<sup>3+</sup>.

***Cyclic Voltammetry of the  $VO^{2+}/VO_2^+$  Redox Couple using N-rGO-Mn<sub>3</sub>O<sub>4</sub>.*** N-rGO-Mn<sub>3</sub>O<sub>4</sub> and Mn<sub>3</sub>O<sub>4</sub> electrodes were prepared by drop-coating suspensions of each material onto GC electrodes to a mass loading of 153  $\mu\text{g cm}^{-2}$ . Figure 5A shows a cyclic voltammogram (CV) obtained at N-rGO-Mn<sub>3</sub>O<sub>4</sub>-coated GC electrode in 1.0 M VOSO<sub>4</sub>/2.0 M H<sub>2</sub>SO<sub>4</sub> at a scan rate ( $\nu$ ) of 30  $\text{mV s}^{-1}$  (red line), which is compared to the response obtained at a bare GC electrode (black line). The general shape of the CVs agrees with that reported previously, with the  $VO^{2+}/VO_2^+$  couple appearing at high potentials and the cathodic formation of  $V^{2+}$  at negative potentials.<sup>52</sup> At bare GC, the peak potential for oxidation of  $VO^{2+}$  to  $VO_2^+$  (Equation 1) was 1.1 V and, during the return sweep, a broad wave appeared, which was centred at 0.6 V and due to the reduction of  $VO_2^+$  to  $VO^{2+}$ . The peak-to-peak separation ( $\Delta E_p$ ) for the  $VO^{2+}/VO_2^+$  redox couple was therefore 0.5 V, which is significantly larger than that expected for oxidation/reduction of a freely-diffusing, reversible redox mediator ( $59/n$  mV, where  $n$  is the number of electrons transferred during the redox reaction<sup>53</sup>), indicating that oxidation/reduction of the  $VO^{2+}/VO_2^+$  redox couple was slow at GC. A large reduction wave appeared at  $-0.5$  V, which is due to the formation of  $V^{2+}$ , but no oxidation peak could be resolved during the return sweep.

Upon changing the electrode material to N-rGO-Mn<sub>3</sub>O<sub>4</sub>, the half-wave potential for the  $VO^{2+}$  oxidation was 0.15 V less positive than at GC, and  $\Delta E_p$  for  $VO^{2+}/VO_2^+$  oxidation/reduction was 0.16 V, which is much smaller than at bare GC. In addition, the half-wave potential for  $V^{2+}$  formation shifted in positive direction by 0.18 V and a small oxidation peak was observed near  $-0.5$  V when using the N-rGO-Mn<sub>3</sub>O<sub>4</sub> electrode. It has been demonstrated previously that the hydrogen evolution reaction (HER;  $H^+ + e^- \rightarrow \frac{1}{2}H_2$ ) coincides with  $V^{2+}$  formation at C electrodes.<sup>54,55</sup> In such situations, the reduction current that flows during the negative sweep is much larger than the oxidation current as C-based

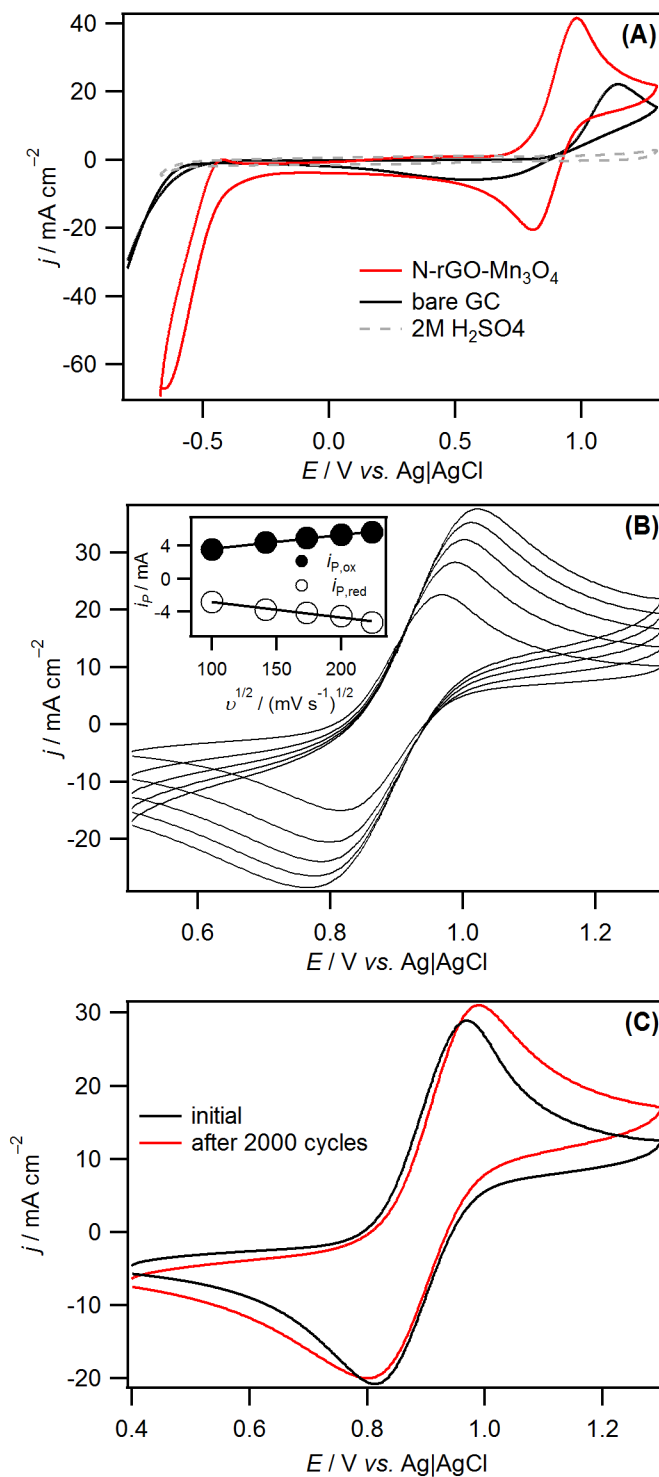


**Figure 5** (A) CVs recorded at a 5-mm diameter bare GC electrode and a GC electrode modified with N-rGO-Mn<sub>3</sub>O<sub>4</sub> at 30 mV s<sup>-1</sup> in 1.0 M VOSO<sub>4</sub>/2.0 M H<sub>2</sub>SO<sub>4</sub> between -0.7 V (initial potential) and 1.3 V for N-rGO-Mn<sub>3</sub>O<sub>4</sub> and between -0.9 V (initial potential) and 1.3 V for bare GC. The dashed line shows the response obtained at the modified GC electrode in blank H<sub>2</sub>SO<sub>4</sub>. (B) CVs obtained at N-rGO-Mn<sub>3</sub>O<sub>4</sub>-modified GC in 1.0 M VOSO<sub>4</sub>/2.0 M H<sub>2</sub>SO<sub>4</sub> at (from top to bottom) 50, 40, 30, 20 and 10 mV s<sup>-1</sup> between 0.5 V (initial potential)

and 1.3 V. (C) CVs recorded in 1.0 M  $VOSO_4$ /2.0 M  $H_2SO_4$  at an N-rGO- $Mn_3O_4$ -modified GC electrode before and after 2000 cycles between 0.4 V (initial potential) and 1.3 V at 500  $mV s^{-1}$ .

electrodes do not catalyse  $H_2$  oxidation effectively. To explore whether the reduction wave observed near  $-0.5$  V in Figure 5A (red line) was partly due to the HER, a CV was recorded at an N-rGO- $Mn_3O_4$  in blank 2.0 M  $H_2SO_4$ . Comparison of the CVs recorded in the blank  $H_2SO_4$  (dashed line in Figure 5A) with that recorded in the presence of vanadium demonstrates that the current was due to  $V^{2+}$  formation rather than the HER. We hypothesised that the lack of a significant oxidation wave during the return (positive sweep) may be due to the existence of a chemical step after electron transfer (a so-called EC mechanism). In such a scenario, and if the species formed during the chemical step is electrochemically inactive within the potential range of the voltammogram, a return wave can be absent, depending on  $\nu$ . It is possible to diagnose the presence of an EC mechanism by varying  $\nu$  and investigating whether the missing return wave reappears at high  $\nu$ , when the voltammetric timescale is sufficiently short that the potential cycle can “outrun” loss of the unstable species. As shown in Figure S4 in the supporting information, the oxidation peak current,  $i_{p,ox}$  increased with increasing  $\nu$ , until the ratio of  $i_{p,ox}$  to the reduction peak current,  $i_{p,red}$ , approached 1 at  $\nu = 200$   $mV s^{-1}$ , confirming that the reduced  $V^{2+}$  species was unstable on the timescale of the slower sweep voltammograms. We also note that Kim *et al.* also recorded a CV with a return oxidation wave during  $V^{2+}$  formation at an  $Mn_3O_4$  electrode, although  $i_{p,ox}/i_{p,red}$  was  $< 1$  and  $\nu$  was not reported so it may be that the reduced species was stable on the timescale of that experiment.<sup>29</sup>

Figure 5B shows the effect of  $\nu$  on the  $VO^{2+}/VO_2^+$  couple using an N-rGO- $Mn_3O_4$ -modified GC electrode. At each  $\nu$ ,  $i_{p,ox}/i_{p,red}$  was near unity and  $i_{p,ox}$  and  $i_{p,red}$  were

proportional to  $v^{1/2}$  (inset of Figure 5B), suggesting that the  $\text{VO}^{2+}/\text{VO}_2^+$  reaction was diffusion-controlled at N-rGO-Mn<sub>3</sub>O<sub>4</sub>. However, the peak potentials showed a clear dependence on  $v$ , suggesting the  $\text{VO}^{2+}/\text{VO}_2^+$  reaction was not completely electrochemically reversible at the N-rGO-Mn<sub>3</sub>O<sub>4</sub>-modified GC electrode. The stability of N-rGO-Mn<sub>3</sub>O<sub>4</sub> for  $\text{VO}^{2+}/\text{VO}_2^+$  electrochemistry was evaluated by an accelerated stability test by cycling the electrode potential 2000 times continuously between 0.4 and 1.3 V. As shown in Figure 5C, after 2000 cycles the composite electrode retained its activity, showing that N-rGO-Mn<sub>3</sub>O<sub>4</sub> is inherently stable during cycling. The remarkable stability of the electrocatalyst under these conditions may be attributable to the interaction between N-rGO and Mn<sub>3</sub>O<sub>4</sub> nanoparticles, hindering dissolution during potential cycling. We note that Kim *et al.* have also developed electrocatalysts consisting of fine Pt nanoparticles dispersed on the surfaces of Mn<sub>3</sub>O<sub>4</sub>, which were stable in acidic media at when cycled to high potentials.<sup>56</sup> In that case, the stability was attributed to the strong metal-Mn<sub>3</sub>O<sub>4</sub> interaction, which prevented loss of the electrocatalyst. In the case of our material, it may be that the anodic stability of Mn<sub>3</sub>O<sub>4</sub> is attributable to an electronic interaction between the N atoms of the doped GO and the Mn<sub>3</sub>O<sub>4</sub>, an effect that also appears responsible for the electrocatalytic activity (as discussed below).

It has been shown previously that the electrocatalytic activity of C-based electrodes for vanadium redox mediators can be enhanced upon doping with N.<sup>16,18,19</sup> The introduction of defect sites upon doping (as demonstrated here using Raman spectroscopy) generates active sites for the adsorption and activation of vanadium ions. Moreover, the negative charge on the N atoms facilitate adsorption of positively-charged vanadium species.<sup>16</sup> The nature of the N species within the carbon framework also impacts on its electrocatalytic activity for vanadium redox reactions. It has been suggested that the presence of lone pair electrons on pyridinic-N and pyrrolic-N species are susceptible to protonation in acidic media,<sup>18</sup> essentially making those N-species inactive for electrocatalysis,<sup>18</sup> In contrast, the

graphitic N-substituted carbon is stable in acidic media as it does not have lone pair of electrons.<sup>18</sup> Therefore, it is possible that the enhanced electrocatalytic activity of the composite material is due to the high graphitic-N (23 %) content of our sample. However, it has also been shown that  $\text{Mn}_3\text{O}_4$  itself can catalyse  $\text{VO}^{2+}/\text{VO}_2^+$ .<sup>29</sup> It could be that the pronounced catalytic activity (and high stability during cycling to high potentials) of N-rGO- $\text{Mn}_3\text{O}_4$  can be explained by synergism between  $\text{Mn}_3\text{O}_4$  and N-rGO. To explore whether such an effect played a role during electrocatalysis, the electrocatalytic activities of free  $\text{Mn}_3\text{O}_4$  and N-rGO were analysed using cyclic voltammetry and electrochemical impedance spectroscopy and compared to that of N-rGO- $\text{Mn}_3\text{O}_4$ . Close examination of the cyclic voltammetry data (Figure 6A) indicates that  $\Delta E_p$  for the  $\text{VO}^{2+}/\text{VO}_2^+$  couple increased from 0.15 V at N-rGO- $\text{Mn}_3\text{O}_4$  to 0.2 V at N-rGO and 0.4 V at  $\text{Mn}_3\text{O}_4$ . The half-wave potential for  $\text{V}^{2+}$  formation also shifted from -0.5 V at N-rGO- $\text{Mn}_3\text{O}_4$  to -0.55 V and -0.6 V at N-rGO and  $\text{Mn}_3\text{O}_4$ , respectively. Moreover, the measured current densities for each redox reaction using the N-rGO- $\text{Mn}_3\text{O}_4$  electrode are significantly higher than those obtained at N-rGO or free  $\text{Mn}_3\text{O}_4$ , indicating that that the composite material had a higher active surface area than either of the individual components.

***Electrochemical Impedance Spectroscopy.*** The electrocatalytic activity of each electrode material towards the  $\text{VO}^{2+}/\text{VO}_2^+$  redox couple was further compared using EIS and Figure 6B shows the resulting Nyquist plots. At each electrode material, Nyquist plot showed one semi-circle within the frequency range of interest and the diameter of the semi-circle represents the charge transfer resistance ( $R_{CT}$ ) of  $\text{VO}^{2+}/\text{VO}_2^+$ . The impedance spectra were fitted to the Randles equivalent circuit by employing the constant phase element (CPE) instead of the double layer capacitor and the results are shown in Table 1. CPE for a rough electrode surface was used as the impedance spectrum of porous electrodes deviates from the

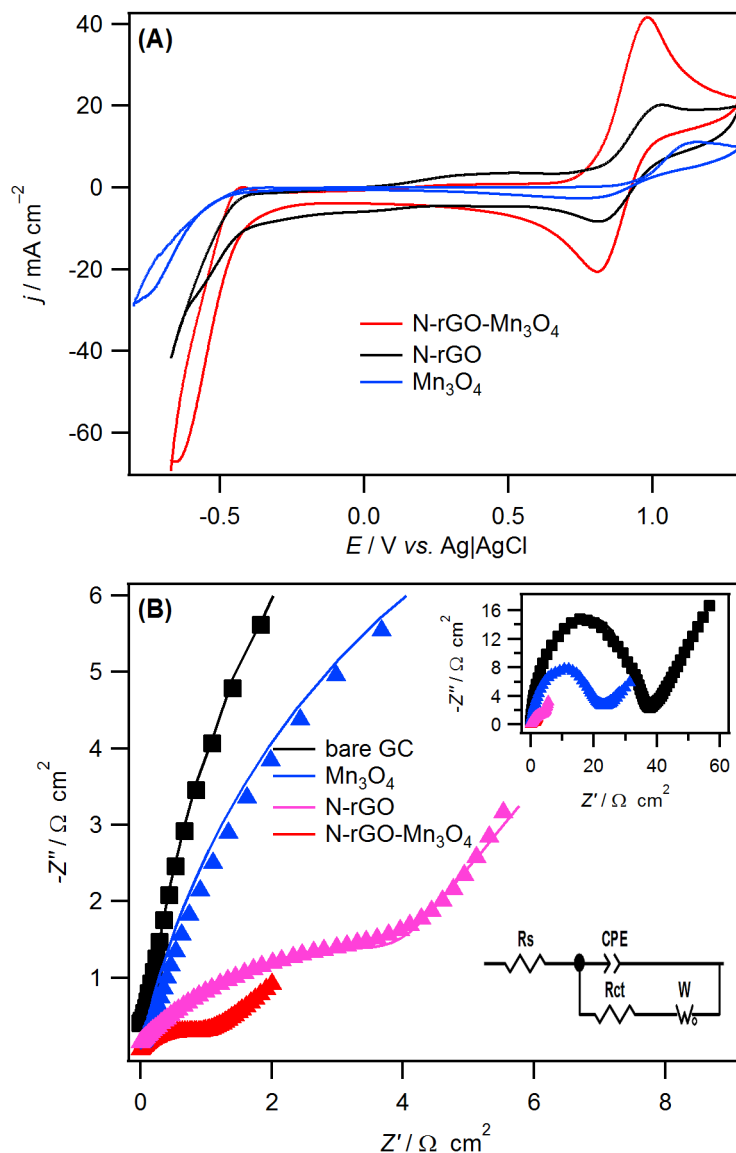


**Figure 6** (A) CVs recorded at N-rGO-Mn<sub>3</sub>O<sub>4</sub>-, N-rGO-, and Mn<sub>3</sub>O<sub>4</sub>-modified GC electrodes at 30 mV s<sup>-1</sup> in 1.0 M VOSO<sub>4</sub>/2.0 M H<sub>2</sub>SO<sub>4</sub> by cycling the potential between -0.7 V (initial) and 1.3 V for both N-rGO-Mn<sub>3</sub>O<sub>4</sub> and N-rGO, and between -0.9 V (initial potential) and 1.3 V for free Mn<sub>3</sub>O<sub>4</sub>. (B) Nyquist plots obtained using the electrodes indicated in A. The measurements were carried out at amplitude of 5 mV in the frequency range 100 mHz - 100 kHz and at an applied potential of 0.95 V. The main frame shows the high frequency region of the plots shown in the upper right inset. The markers show the experimental data and the solid lines show theoretical fits generated using the equivalent circuit shown in lower right inset. For clarity each curve was shifted to zero on the x-axis

**Table 1.** EIS parameters extracted from theoretical fits to the Randles equivalent circuit obtained using various electrodes

Electrodes	$R_s / \Omega \text{ cm}^2$	$R_{CT} / \Omega \text{ cm}^2$	$W / \Omega \text{ cm}^2$	$Q / \mu\text{F cm}^{-2} \text{ s}^{-\beta}$	$\beta$
N-rGO-Mn <sub>3</sub> O <sub>4</sub>	2.1	1.1	22.3	400	0.6
Bare GC	2.3	35	16.7	21.4	0.9
Mn <sub>3</sub> O <sub>4</sub>	2.4	19	56	20	0.85
N-rGO	2.5	6.3	122	500	0.5

behaviour of an ideal capacitor.<sup>57-59</sup> The impedance of CPE is given by  $Z_{CPE} = \frac{1}{Q(i\omega)^\beta}$ , where  $\omega$  is the angular frequency,  $i$  in this case is the imaginary unit,  $Q$  is the CPE pre-factor, and  $\beta$  is its exponent ( $0 \leq \beta \leq 1$ ).<sup>60</sup> The deviation from an ideal capacitance at bare GC was small and the values for  $\beta$  were not smaller than 0.9 and can be neglected for the determination of the double layer capacitance. However, at N-rGO-Mn<sub>3</sub>O<sub>4</sub> and N-rGO, the deviation from an ideal capacitance was more pronounced with  $\beta$  values of less than 0.7. In addition, and as expected, the diffusion impedances within the porous N-rGO and Mn<sub>3</sub>O<sub>4</sub> films were higher than that at the bare GC but, notably, that of the composite material was lower than that of either the N-rGO or the Mn<sub>3</sub>O<sub>4</sub> alone. The trend in the  $R_{CT}$  values shows that charge transfer was significantly faster at the N-rGO-Mn<sub>3</sub>O<sub>4</sub> surface than at the other surfaces, which is consistent with the cyclic voltammetry data.

***Effect of N-Doping and Mn<sub>3</sub>O<sub>4</sub> Loading on Electrocatalytic Activity.*** Both the CV and EIS data demonstrate that the N-rGO-Mn<sub>3</sub>O<sub>4</sub> composite is electrocatalytically more active than either N-rGO or Mn<sub>3</sub>O<sub>4</sub> alone. We also studied undoped rGO-Mn<sub>3</sub>O<sub>4</sub> to examine the effect of omitting N from the composite on the electrocatalysis. As shown in Figure S5 in the Supporting Information, the composite material with no N shows very little activity for the redox process. This indicates that N plays a crucial role and that the synergistic effects observed are due to the strong electronic coupling within the composite *via* the formation of Mn-N-C bond in N-rGO-Mn<sub>3</sub>O<sub>4</sub>.<sup>30,34</sup>

The effects of changing the loading of Mn<sub>3</sub>O<sub>4</sub> on N-rGO were studied by TGA and cyclic voltammetry. Some slight weight losses were observed below 100 °C during TGA (Figure 7A), which can be attributed to the removal of physically-adsorbed water molecules. The weight loss between 250 °C and 480 °C is attributed to removal of the residual oxygen groups from the surface of N-rGO and the subsequent decomposition of the carbon skeleton.<sup>61</sup> The decomposition temperature of rGO shifted to lower temperatures as the extent of Mn<sub>3</sub>O<sub>4</sub> loading increased from 10 wt.% to 46 wt.%, showing that Mn<sub>3</sub>O<sub>4</sub> catalyses the decomposition of rGO. The work of Zhang *et. al.*<sup>18</sup> suggests the electrocatalytic activity of N-doped graphene is determined by the type of N species in the graphene sheets and not by the concentration of N. While keeping the N concentration constant, we studied the effect of the Mn<sub>3</sub>O<sub>4</sub> loading on the electrocatalytic performance and found that a 10% loading of Mn<sub>3</sub>O<sub>4</sub> (Figure 7B) resulted in a poor electrocatalytic activity. As the amount of Mn<sub>3</sub>O<sub>4</sub> increased from 10 wt.% to 46 wt.%, the onset potential for the formation of V<sup>2+</sup> shifted progressively towards less negative potentials and the VO<sup>2+</sup> oxidation current increased. This implies that the active site in the hybrid material may be at the interface of Mn<sub>3</sub>O<sub>4</sub> and N-rGO, as also suggested by previous work on synergistic graphene-Co<sub>3</sub>O<sub>4</sub> electrocatalysts for O<sub>2</sub> reduction,<sup>30</sup> and that electron transfer between the N atoms and the metal electrocatalyst

facilitates electron transfer during electrocatalysis. However, once the  $\text{Mn}_3\text{O}_4$  loading passed 25 wt %,  $\Delta E_p$  for  $\text{VO}^{2+}/\text{VO}_2^+$  slightly, presumably increased due to the increasing film resistance.

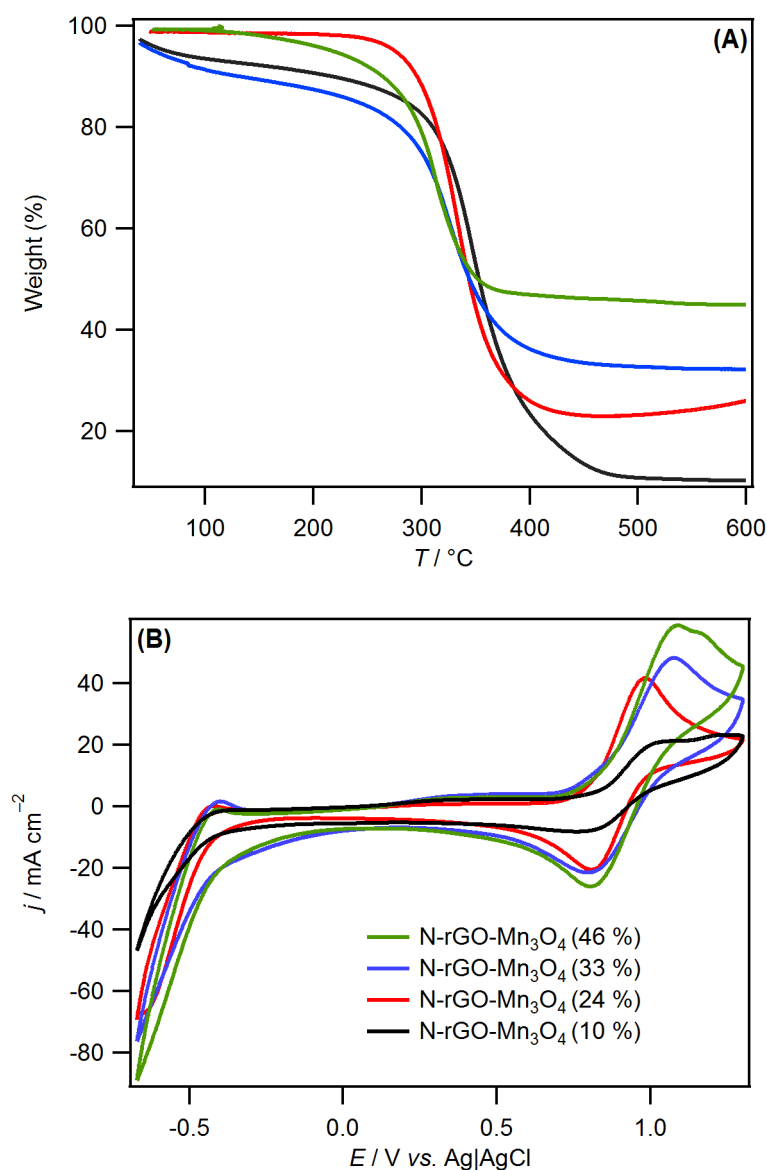


**Figure 7** (A) TGA traces recorded for various N-rGO-Mn<sub>3</sub>O<sub>4</sub> samples obtained by ramping the temperature from 40 °C to 600 °C at a rate of 10 °C min<sup>-1</sup> in air. The colour scheme is as indicated in the lower figure. (B) CVs recorded using various N-rGO-Mn<sub>3</sub>O<sub>4</sub>-modified electrodes at 30 mV s<sup>-1</sup> in 1.0 M VOSO<sub>4</sub>/2.0 M H<sub>2</sub>SO<sub>4</sub> by cycling the potential between -0.7 V (initial potential) and 1.3 V.

## Conclusions

The electrocatalytic activity of a composite N-doped, reduced graphene oxide/Mn<sub>3</sub>O<sub>4</sub> electrocatalyst towards the VO<sup>2+</sup>/VO<sub>2</sub><sup>+</sup> redox couple in aqueous media has been studied using cyclic voltammetry and electrochemical impedance spectroscopy. The activity of N-rGO-Mn<sub>3</sub>O<sub>4</sub> is higher than that of the free Mn<sub>3</sub>O<sub>4</sub> and N-rGO alone, due to a synergistic coupling between N-rGO and Mn<sub>3</sub>O<sub>4</sub>. The synergistic effect is only apparent when N is incorporated into the carbon framework of the graphene support, showing that the metal-nitrogen-carbon interaction is key to the performance of the electrocatalyst. The optimum Mn<sub>3</sub>O<sub>4</sub> loading is ~24 % but, at higher Mn<sub>3</sub>O<sub>4</sub> loadings, the performance decreases due to an increase in film resistance. Our identification of the benefits of electrocatalyst-support interactions could lead to new directions in the development of novel electrocatalysts for RFBs. Identification of similar synergistic electrocatalyst-support interactions in Earth-abundant electrocatalysts for V<sup>3+</sup>/V<sup>2+</sup> electrochemistry may lead to the development of new high-performance, fully-functional all-vanadium RFBs and future efforts will focus on this challenge.

## Acknowledgements

We thank the Leverhulme Trust (Project RPG-2010-510) for support.

## Supporting Information

SEM image of GO, TEM image of Mn<sub>3</sub>O<sub>4</sub>, O 1s XP spectrum of N-rGO-Mn<sub>3</sub>O<sub>4</sub>, chemical compositions of GO and N-rGO-Mn<sub>3</sub>O<sub>4</sub>, cyclic voltammograms of N-rGO-Mn<sub>3</sub>O<sub>4</sub> at various scan rates, and cyclic voltammograms of N-rGO-Mn<sub>3</sub>O<sub>4</sub> compared to rGO-Mn<sub>3</sub>O<sub>4</sub>. This information is available free of charge via the Internet at <http://pubs.acs.org/>.

## References

- (1) Alotto, P.; Guarnieri, M.; Moro, F. *Renew. Sust. Energy Rev.* **2014**, *29*, 325-335.
- (2) Guo, Y. G.; Hu, J. S.; Wan, L. J. *Adv. Mater* **2008**, *20*, 2878-2887.
- (3) Carmo, M.; Fritz, D. L.; Mergel, J.; Stolten, D. *Int. J. Hydrogen Energy* **2013**, *38*, 4901-4934.
- (4) Etacheri, V.; Marom, R.; Elazari, R.; Salitra, G.; Aurbach, D. *Energy Environ. Sci.* **2011**, *4*, 3243-3262.
- (5) Yang, Z. G.; Zhang, J. L.; Kintner-Meyer, M. C. W.; Lu, X. C.; Choi, D. W.; Lemmon, J. P.; Liu, J. *Chem. Rev.* **2011**, *111*, 3577-3613.
- (6) Ponce de Leon, C.; Frias-Ferrer, A.; Gonzalez-Garcia, J.; Szanto, D. A.; Walsh, F. C. *J. Power Sources* **2006**, *160*, 716-732.
- (7) Skyllas-Kazacos, M.; Chakrabarti, M. H.; Hajimolana, S. A.; Mjalli, F. S.; Saleem, M. *J. Electrochem. Soc.* **2011**, *158*, R55-R79.
- (8) Rahman, F.; Skyllas-Kazacos, M. *J. Power Sources* **2009**, *189*, 1212-1219.
- (9) Shin, S. H.; Yun, S. H.; Moon, S. H. *RSC Adv.* **2013**, *3*, 9095-9116.
- (10) Ejigu, A.; Greatorex-Davies, P. A.; Walsh, D. A. *Electrochem. Commun.* **2015**, *54*, 55-59.
- (11) Skyllas-Kazacos, M.; Rychcik, M.; Robins, R. G.; Fane, A. G.; Green, M. A. *J. Electrochem. Soc.* **1986**, *133*, 1057-1058.
- (12) Kim, K. J.; Park, M.-S.; Kim, Y.-J.; Kim, J. H.; Dou, S. X.; Skyllas-Kazacos, M. *J. Mater. Chem. A* **2015**, *3*, 16913-16933.
- (13) Park, M.; Ryu, J.; Cho, J. *Chem. Asian J.* **2015**, *10*, 2096-2110.

- (14) Parasuraman, A.; Lim, T. M.; Menictas, C.; Skyllas-Kazacos, M. *Electrochim. Acta* **2013**, *101*, 27-40.
- (15) Rychcik, M.; Skyllas-Kazacos, M. *J. Power Sources* **1987**, *19*, 45-54.
- (16) Park, M.; Ryu, J.; Kim, Y.; Cho, J. *Energy Environ. Sci.* **2014**, *7*, 3727-3735.
- (17) Wang, S.; Zhao, X.; Cochell, T.; Manthiram, A. *J. Phys. Chem. Lett.* **2012**, *3*, 2164-2167.
- (18) Jin, J. T.; Fu, X. G.; Liu, Q.; Liu, Y. R.; Wei, Z. Y.; Niu, K. X.; Zhang, J. Y. *ACS Nano* **2013**, *7*, 4764-4773.
- (19) Shao, Y.; Wang, X.; Engelhard, M.; Wang, C.; Dai, S.; Liu, J.; Yang, Z.; Lin, Y. *J. Power Sources* **2010**, *195*, 4375-4379.
- (20) Han, P.; Wang, H.; Liu, Z.; Chen, X.; Ma, W.; Yao, J.; Zhu, Y.; Cui, G. *Carbon* **2011**, *49*, 693-700.
- (21) Kim, K. J.; Kim, Y.-J.; Kim, J.-H.; Park, M.-S. *Mater. Chem. Phys.* **2011**, *131*, 547-553.
- (22) Han, P.; Yue, Y.; Liu, Z.; Xu, W.; Zhang, L.; Xu, H.; Dong, S.; Cui, G. *Energy Environ. Sci.* **2011**, *4*, 4710-4717.
- (23) Han, P.; Wang, X.; Zhang, L.; Wang, T.; Yao, J.; Huang, C.; Gu, L.; Cui, G. *RSC Adv.* **2014**, *4*, 20379-20381.
- (24) Li, W.; Liu, J.; Yan, C. *Carbon* **2013**, *55*, 313-320.
- (25) Yue, L.; Li, W.; Sun, F.; Zhao, L.; Xing, L. *Carbon* **2010**, *48*, 3079-3090.
- (26) Ding, C.; Zhang, H.; Li, X.; Liu, T.; Xing, F. *J. Phys. Chem. Lett.* **2013**, *4*, 1281-1294.

- (27) Li, B.; Gu, M.; Nie, Z.; Wei, X.; Wang, C.; Sprenkle, V.; Wang, W. *Nano Lett.* **2014**, *14*, 158-165.
- (28) Yao, C.; Zhang, H.; Liu, T.; Li, X.; Liu, Z. *J. Power Sources* **2012**, *218*, 455-461.
- (29) Kim, K. J.; Park, M.-S.; Kim, J.-H.; Hwang, U.; Lee, N. J.; Jeong, G.; Kim, Y.-J. *Chem. Commun.* **2012**, *48*, 5455-5457.
- (30) Liang, Y.; Li, Y.; Wang, H.; Zhou, J.; Wang, J.; Regier, T.; Dai, H. *Nat. Mater.* **2011**, *10*, 780-786.
- (31) Cargnello, M.; Doan-Nguyen, V. V. T.; Gordon, T. R.; Diaz, R. E.; Stach, E. A.; Gorte, R. J.; Fornasiero, P.; Murray, C. B. *Science* **2013**, *341*, 771-773.
- (32) Chen, S.; Duan, J.; Jaroniec, M.; Qiao, S.-Z. *Adv. Mater.* **2014**, *26*, 2925-2930.
- (33) Xiao, J.; Bian, X.; Liao, L.; Zhang, S.; Ji, C.; Liu, B. *ACS Appl. Mater. Interfaces* **2014**, *6*, 17654-17660.
- (34) Liang, Y.; Wang, H.; Zhou, J.; Li, Y.; Wang, J.; Regier, T.; Dai, H. *J. Am. Chem. Soc.* **2012**, *134*, 3517-3523.
- (35) Marcano, D. C.; Kosynkin, D. V.; Berlin, J. M.; Sinitskii, A.; Sun, Z. Z.; Slesarev, A.; Alemany, L. B.; Lu, W.; Tour, J. M. *ACS Nano* **2010**, *4*, 4806-4814.
- (36) Bag, S.; Roy, K.; Gopinath, C. S.; Raj, C. R. *ACS Appl. Mater. Interfaces* **2014**, *6*, 2692-2699.
- (37) Stankovich, S.; Dikin, D. A.; Piner, R. D.; Kohlhaas, K. A.; Kleinhammes, A.; Jia, Y.; Wu, Y.; Nguyen, S. T.; Ruoff, R. S. *Carbon* **2007**, *45*, 1558-1565.
- (38) Yang, H.; Jiang, J.; Zhou, W.; Lai, L.; Xi, L.; Lam, Y. M.; Shen, Z.; Khezri, B.; Yu, T. *Nanoscale Res. Lett.* **2011**, *6*, 531.

- (39) Du, J.; Gao, Y. Q.; Chai, L. L.; Zou, G. F.; Li, Y.; Qian, Y. T. *Nanotechnology* **2006**, *17*, 4923-4928.
- (40) Boutchich, M.; Jaffré, A.; Alamarguy, D.; Alvarez, J.; Barras, A.; Tanizawa, Y.; Tero, R.; Okada, H.; Thu, T. V.; Kleider, J. P.; Sandhu, A. *J. Physics: Conf. Series* **2013**, *433*, 012001.
- (41) Zou, Y. Q.; Kinloch, I. A.; Dryfe, R. A. W. *J. Mater. Chem. A* **2014**, *2*, 19495-19499.
- (42) Geng, D. S.; Yang, S. L.; Zhang, Y.; Yang, J. L.; Liu, J.; Li, R. Y.; Sham, T. K.; Sun, X. L.; Ye, S. Y.; Knights, S. *Appl. Surface Sci.* **2011**, *257*, 9193-9198.
- (43) Zuo, J.; Xu, C. Y.; Liu, Y. P.; Qian, Y. T. *Nanostruct. Mater.* **1998**, *10*, 1331-1335.
- (44) Duan, J.; Zheng, Y.; Chen, S.; Tang, Y.; Jaroniec, M.; Qiao, S. *Chem. Commun.* **2013**, *49*, 7705-7707.
- (45) Wang, H.; Maiyalagan, T.; Wang, X. *ACS Catalysis* **2012**, *2*, 781-794.
- (46) Sheng, Z.-H.; Shao, L.; Chen, J.-J.; Bao, W.-J.; Wang, F.-B.; Xia, X.-H. *ACS Nano* **2011**, *5*, 4350-4358.
- (47) Raj, A. M. E.; Victoria, S. G.; Jothy, V. B.; Ravidhas, C.; Wollschlager, J.; Suendorf, M.; Neumann, M.; Jayachandran, M.; Sanjeeviraja, C. *Appl. Surface Sci.* **2010**, *256*, 2920-2926.
- (48) Nesbitt, H. W.; Banerjee, D. *Am. Miner.* **1998**, *83*, 305-315.
- (49) Park, S. K.; Jin, A.; Yu, S. H.; Ha, J.; Jang, B.; Bong, S.; Woo, S.; Sung, Y. E.; Piao, Y. *Electrochim. Acta* **2014**, *120*, 452-459.
- (50) Chigane, M.; Ishikawa, M. *J. Electrochem. Soc.* **2000**, *147*, 2246-2251.

- (51) Murugan, B.; Ramaswamy, A. V.; Srinivas, D.; Gopinath, C. S.; Ramaswamy, V. *Chem. Mater.* **2005**, *17*, 3983-3993.
- (52) Sun, B.; Skyllas-Kazakos, M. *Electrochim. Acta* **1991**, *36*, 513-517.
- (53) Bard, A. J.; Faulkner, L. R. *Electrochemical Methods: Fundamentals and Applications*; 2<sup>nd</sup> ed., John Wiley & Sons, Hoboken, New Jersey, 2001, p. 241.
- (54) Sun, C. N.; Delnick, F. M.; Baggetto, L.; Veith, G. M.; Zawodzinski, T. A. *J. Power Sources* **2014**, *248*, 560-564.
- (55) Shah, A. A.; Al-Fetlawi, H.; Walsh, F. C. *Electrochim. Acta* **2010**, *55*, 1125-1139.
- (56) Kim, K. W.; Kim, S. M.; Choi, S.; Kim, J.; Lee, I. S. *ACS Nano* **2012**, *6*, 5122-5129.
- (57) Hauch, A.; Georg, A. *Electrochim. Acta* **2001**, *46*, 3457-3466.
- (58) Zistler, M.; Schreiner, C.; Wachter, P.; Wassercheid, P.; Gerhard, D.; Gores, H. J. *Int. J. Electrochem. Sci.* **2008**, *3*, 236-245.
- (59) Kawano, R.; Matsui, H.; Matsuyama, C.; Sato, A.; Susan, M.; Tanabe, N.; Watanabe, M. *J. Photochem. Photobiol. A-Chem.* **2004**, *164*, 87-92.
- (60) Macdonald, J. R.; Johnson, W. B. In *Impedance Spectroscopy: Theory, Experiment, and Applications*; Barsoukov, E., Macdonald, J. R., Eds., John Wiley & Sons, Hoboken, New Jersey, 2005, p 18.
- (61) Zhang, J.; Jiang, J.; Zhao, X. S. *J. Phy. Chem. C* **2011**, *115*, 6448-6454.

## Graphical Abstract

